scientific reports

Check for updates

OPEN

Experimental study on seepage characteristics model of tunnel lining based on infrared imaging

Zhijian Wu[1], Hua Wu[2], Yichen Peng[3], Renjie Song[3], Yimin Wu[2,3]✉, Haiping Wu[3] & Guangzheng Zhuang[3]

Lining seepage is one of the most prevalent structural diseases in tunnel engineering. The variability of lining crack types and the complexity of groundwater seepage conditions pose significant threats to tunnel safety and operational integrity. Most previous studies have focused primarily on the geometric characteristics of seepage areas, while the relationships between these geometric features and other influencing factors, as well as the development of quantitative indicators within infrared signatures for rapid crack pattern identification, have not been systematically explored. To investigate the influence of secondary lining crack patterns and seepage rate on infrared characteristics of seepage, this research innovatively creates a custom-designed seepage simulation device for tunnel secondary linings, and systematic studies on infrared features of seepage were conducted. The results show that: (1) Geometric characteristics of seepage areas for various crack types were systematically summarized, where crack patterns and their positions determine the geometric features of seepage regions; (2) Seepage areas of all crack types increase with flow rate, and different crack morphologies exhibit distinct susceptibility to flow rate at varied positions; (3) The centroid distance curve of the seepage core area derived from isothermal maps enables rapid identification of crack morphologies and their positions within the tunnel by analyzing curve patterns. This research lays a foundational basis for the rapid identification of water seepage areas in infrared detection technology for tunnel water leakage, while also providing theoretical support for promoting the transition from qualitative to quantitative analysis of water seepage areas in current infrared detection practices.

Keywords Tunnel seepage, Lining crack, Infrared identification, Temperature field

In tunnel engineering, seepage in tunnel linings is one of the common diseases. Long-term seepage not only threatens the safety and durability of the structure[1–4], but may also seriously affect the traffic function and service life of facilities inside the tunnel[5,6]. Therefore, the detection and identification of tunnel lining seepage are particularly important[7–9]. Traditional detection methods for tunnel lining seepage mainly rely on means such as visual inspection and periodic monitoring[10–13]. Although these methods are simple and feasible, due to the complex background of the tunnel lining surface, according to Technical Specification for Construction of Highway Asphalt Pavements (JTG F40-2004)[14], the wet area refers to a surface with non-flowing wetness caused by condensation, micro-seepage, or ambient humidity (without standing water), while the seepage area refers to a surface with continuous water exudation (either from active drainage or passive leakage), coupled with the similar colors of the seepage area and the wet area, it is difficult to effectively distinguish between the seepage area and the wet area[15,16]. Especially when long-term monitoring of large-scale tunnels is carried out, there are great limitations, and this manual detection method is inefficient[17–20]. Therefore, with the continuous expansion of tunnel construction scale and the improvement of monitoring requirements, traditional detection methods have been difficult to meet the accuracy and efficiency requirements of modern tunnel engineering for seepage detection[21–23].

To effectively distinguish between wet surfaces and seepage areas, and to rapidly determine the crack morphology causing seepage, it is necessary to apply infrared thermal imaging technology in the detection and identification of tunnel lining seepage[24,25]. Infrared thermal imaging technology utilizes the principle of infrared radiation to reveal temperature differences caused by seepage by detecting the temperature distribution on the object surface. Seepage induces changes in the thermal conductivity of lining materials, manifesting as

[1]Jiangxi Communications Investment Group Co., Ltd, Nanchang 330025, Jiangxi, China. [2]Anhui Transport Consulting & Design Institute Co., Ltd, Hefei 230088, Anhui, China. [3]School of Civil Engineering, Central South University, Changsha 410075, Hunan, China. ✉email: wuyimin531@csu.edu.cn

temperature anomalies in infrared thermal images[26,27]. Thus, infrared thermal imaging can effectively identify seepage areas, particularly with high detection accuracy and wide applicability based on non-destructive testing. Wu Hangbin et al.[28] effectively identified and localized tunnel seepage areas using near-infrared thermal imaging combined with morphological filtering and isotherm extraction techniques. Dou Haitao et al.[29] studied the temperature distribution characteristics of point-like seepage and their relationship with seepage positions through simulating the seepage process of tunnel linings. Zheng Aichen et al.[30] further analyzed the influence of different defect forms on the seepage temperature field in a simulated tunnel environment, providing a basis for the preliminary determination of seepage areas.

Although existing studies have demonstrated the significant potential of infrared thermal imaging technology in seepage detection, due to the diversity of tunnel lining crack morphologies, the concealment of seepage positions, and the complexity of groundwater flow, there is still a lack of quantitative research on the characteristics of seepage areas[31–33]. Therefore, through a self-developed lining seepage simulation device combined with infrared thermal imaging technology, this study conducts an in-depth analysis of the geometric characteristics and temperature field distribution of seepage points under different crack morphologies, seepage positions, and flow conditions. By analyzing the centroid distance curves of the seepage temperature field, the seepage characteristics of seepage cracks with four different morphologies in the secondary lining at three different positions (vault, spandrel, and haunch) have been quantified to a certain extent, providing valuable reference quantitative indicators. Through the systematic study of these factors, it aims to provide more scientific and precise theoretical support for the intelligent recognition technology of infrared images of tunnel lining surface seepage, thereby promoting the application and development of this technology in tunnel seepage detection.

Simulation test of seepage from cracked secondary tunnel lining

To investigate the relationships between factors such as the geometric, thermal, and positional characteristics of seepage and the morphology of lining cracks, a simulation test of seepage from cracked secondary tunnel linings was conducted using an infrared camera.

Specimen design and fabrication

The specimen was designed as an arc-shaped concrete slab to simulate the tunnel lining structure, with a thickness of 10 cm, a circumferential arc length of 1.2 m, and a longitudinal length of 1.2 m. The concrete specimen was reinforced with longitudinal and circumferential threaded steel bars with a diameter of 8 mm at a spacing of 200 mm × 200 mm, and 6 mm threaded steel bars were used as stirrups. The steel bars were all of HRB400 grade. The design diagram of the specimen is shown in Fig. 1. The mix ratio of the cast concrete was designed according to the strength of C35 grade concrete.

Test environment construction

The real tunnel seepage environment is simulated by a self-developed tunnel lining seepage simulation device and water temperature/flow control system, as shown in Fig. 2. The test equipment is mainly composed of an infrared camera, metering pump, temperature controller, lifting device, water bucket, etc. The infrared camera is a Hikvision K20 camera, with a distance of 60 cm from the camera to the surface of the tested concrete specimen

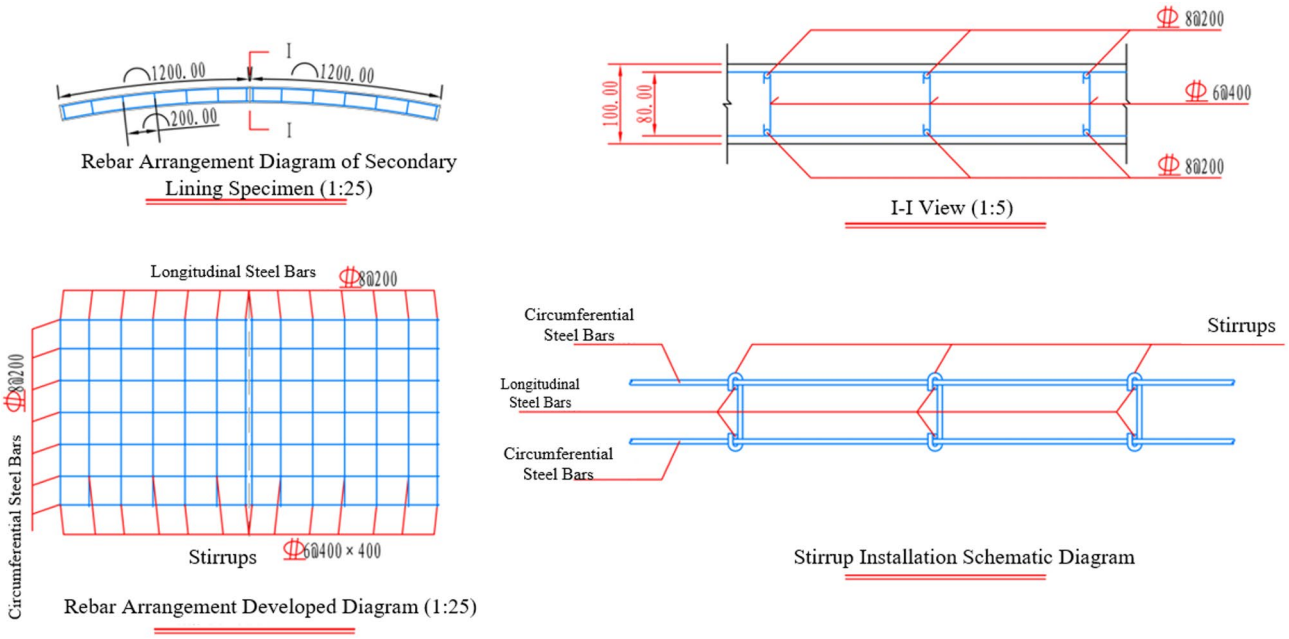

Fig. 1. Design diagram of lining seepage specimen.

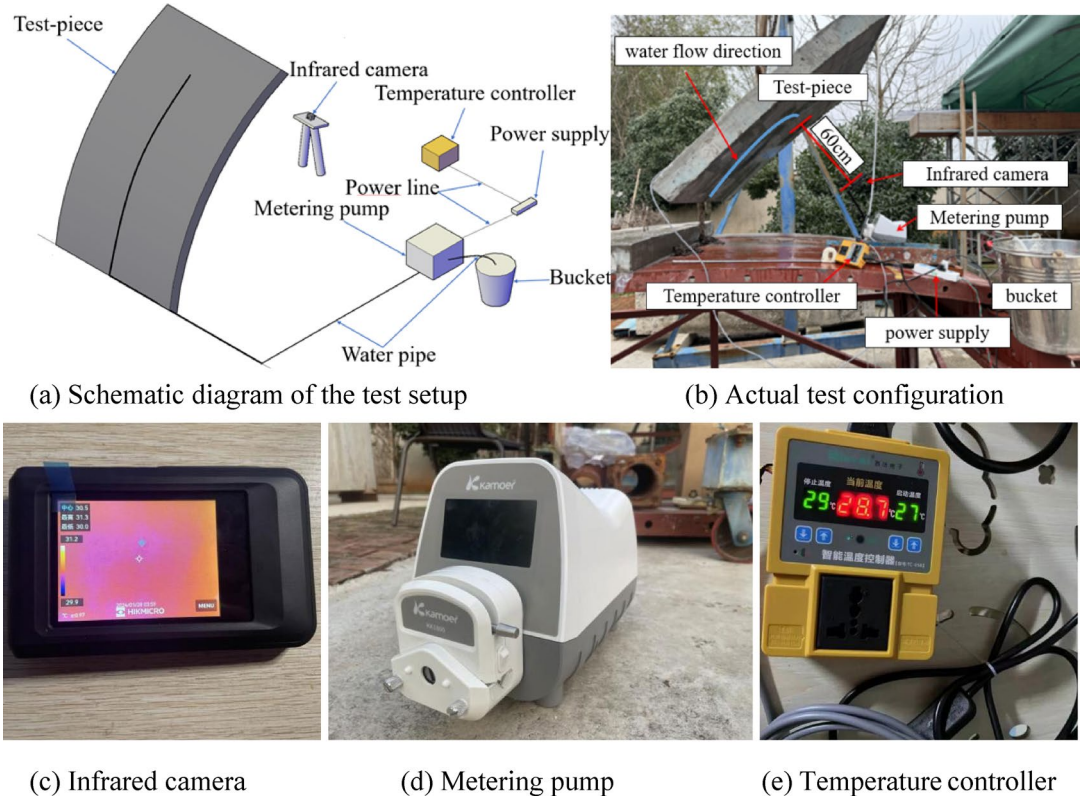

Fig. 2. Test setup.

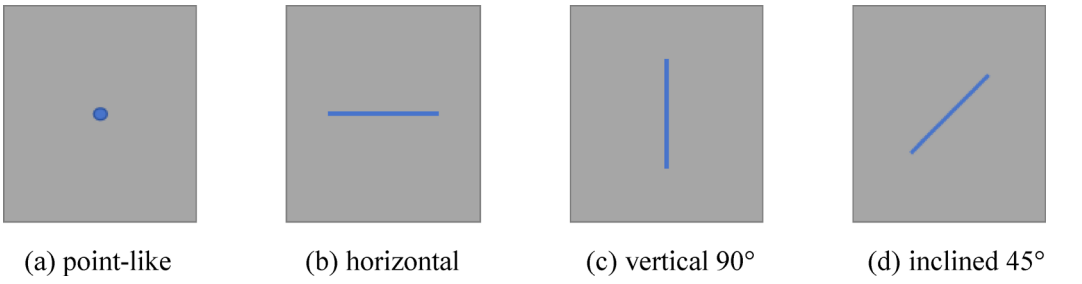

Fig. 3. Design of tunnel lining crack morphologies.

and a temperature measurement range of − 20 to 400 °C, from the perspective of the camera, the direction of water flow will seep in a 90-degree vertical direction. The metering pump is a Kamoer DIP1500 flowmeter-displayed constant current pump. The temperature controller uses a Xifa PID constant temperature controller.

Test conditions setting

The specimen was designed with four types of cracks according to the common morphologies of tunnel linings: point-like (6 mm diameter), linear (horizontal 180°, 1.5 × 15 mm), linear (vertical 90°, 1.5 × 15 mm), and linear (inclined 45°, 1.5 × 15 mm), as shown in Fig. 3. Point-like defects were created by drilling with an electric drill after concrete casting and curing. Linear cracks were fabricated by embedding steel plates in the formwork, and the specimen fabrication process is illustrated in Fig. 4. As shown in Fig. 4b, four U-shaped steel bars were welded around the steel reinforcement cage before casting, enabling angle adjustment of the specimen via a lifting device after casting.

After the fabrication of the specimen, the method for simulating the vault, spandrel, and haunch is illustrated in Fig. 5.

Test procedures

The specimen was lifted and adjusted to the corresponding lining position using a lifting device. Ambient temperature was maintained at 25 ± 1 °C in a constant-temperature laboratory, and humidity was controlled at 60 ± 5% to prevent condensation from affecting infrared imaging. The specimen surface was polished and

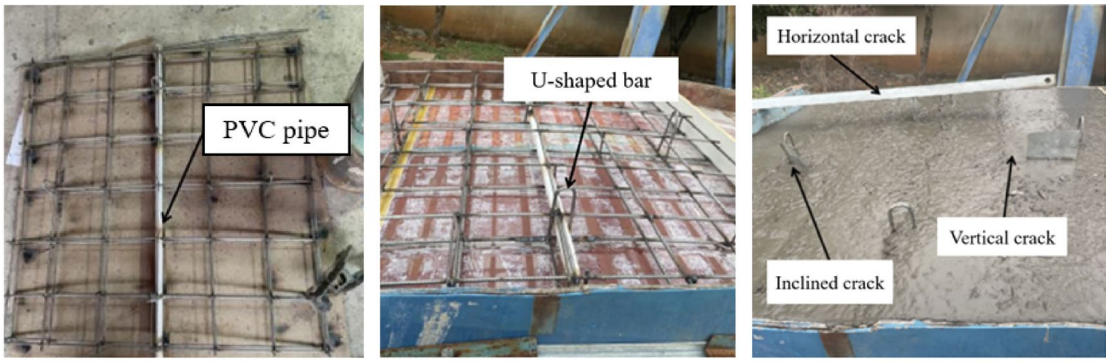

Fig. 4. Fabrication process of tunnel crack lining specimen.

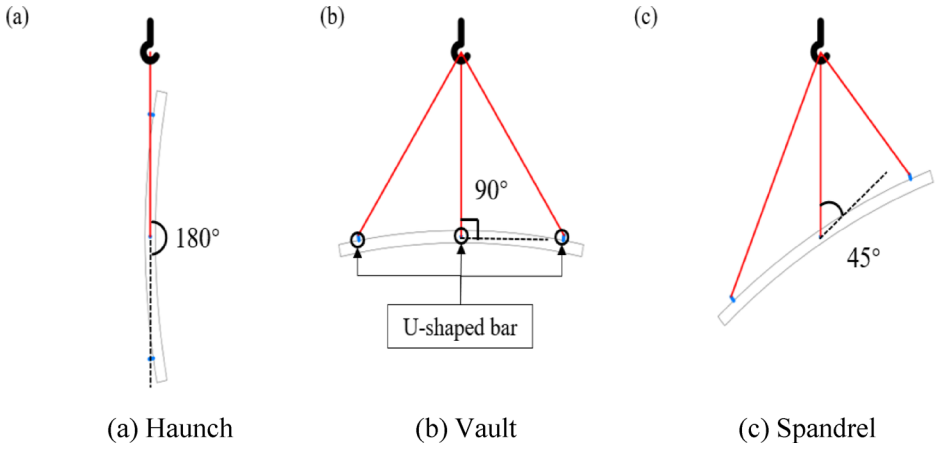

Fig. 5. Schematic diagram of lifting scheme.

cleaned to remove dust and impurities, ensuring stable thermal radiation signals. A constant-temperature controller was used to precisely regulate the water flow temperature at 20 ± 0.5 °C, minimizing the interference of water temperature fluctuations on the temperature field. A windproof isolation hood was installed in the test area to avoid surface temperature disturbances caused by air flow. And a silicone tube was inserted into the corresponding crack for water injection, with the flow rate regulated by a metering pump. The infrared camera was fixed on a bracket 60 cm in front of the cracked area, maintaining perpendicularity to the specimen surface. One point-like crack, one vertical crack, one inclined crack, and one horizontal crack were each fabricated on the specimen, resulting in a total of four cracks. Tests were conducted under four different flow rates at three positions (vault, spandrel, and haunch), leading to a total of 48 test conditions, as detailed in Table 1. Each test condition captured images at 5-second intervals for 1 min.

Geometric characteristics analysis of tunnel lining seepage

Geometric characteristics of seepage areas under different crack morphologies

To provide a theoretical basis for rapid and quantitative identification of tunnel lining seepage, the geometric characteristics of seepage were analyzed, and infrared thermal images of seepage areas under different crack morphologies were plotted, as shown in Fig. 6.

Geometric characteristics of seepage area with point-like cracks

Infrared thermal images of the seepage area under point-like crack conditions are shown in Fig. 6a. The seepage area of point-like defects at the vault expands outward with increasing flow rate, presenting a circular shape. The seepage area of point-like cracks at the spandrel shows a uniform-width strip distribution below the seepage point and a semicircular distribution at the top. As the flow rate increases, the horizontal width of the seepage area increases, forming a bullet-like shape overall. The seepage tributaries below the image occur due to depressions in the concrete specimen. At the haunch, the seepage area of point-like defects still shows a semicircular distribution at the top, similar to that at the spandrel. As the seepage path increases from the seepage point downward, the horizontal seepage area expands, presenting a mountain-like shape overall.

Condition	Lining position	Crack type	Flow rate (mL/min)
1	Vault	Point-like crack (6 mm)	300, 600, 900, 1200
2		Inclined linear crack (1.5 × 15 mm)	300, 600, 900, 1200
3		Vertical linear crack (1.5 × 15 mm)	300, 600, 900, 1200
4		Horizontal linear crack (1.5 × 15 mm)	300, 600, 900, 1200
5	Spandrel	Point-like crack (6 mm)	300, 600, 900, 1200
6		Inclined linear crack (1.5 × 15 mm)	300, 600, 900, 1200
7		Vertical linear crack (1.5 × 15 mm)	300, 600, 900, 1200
8		Horizontal linear crack (1.5 × 15 mm)	300, 600, 900, 1200
9	Haunch	Point-like crack (6 mm)	300, 600, 900, 1200
10		Inclined linear crack (1.5 × 15 mm)	300, 600, 900, 1200
11		Vertical linear crack (1.5 × 15 mm)	300, 600, 900, 1200
12		Horizontal linear crack (1.5 × 15 mm)	300, 600, 900, 1200

Table 1. Test conditions for seepage simulation of cracked secondary tunnel linings.

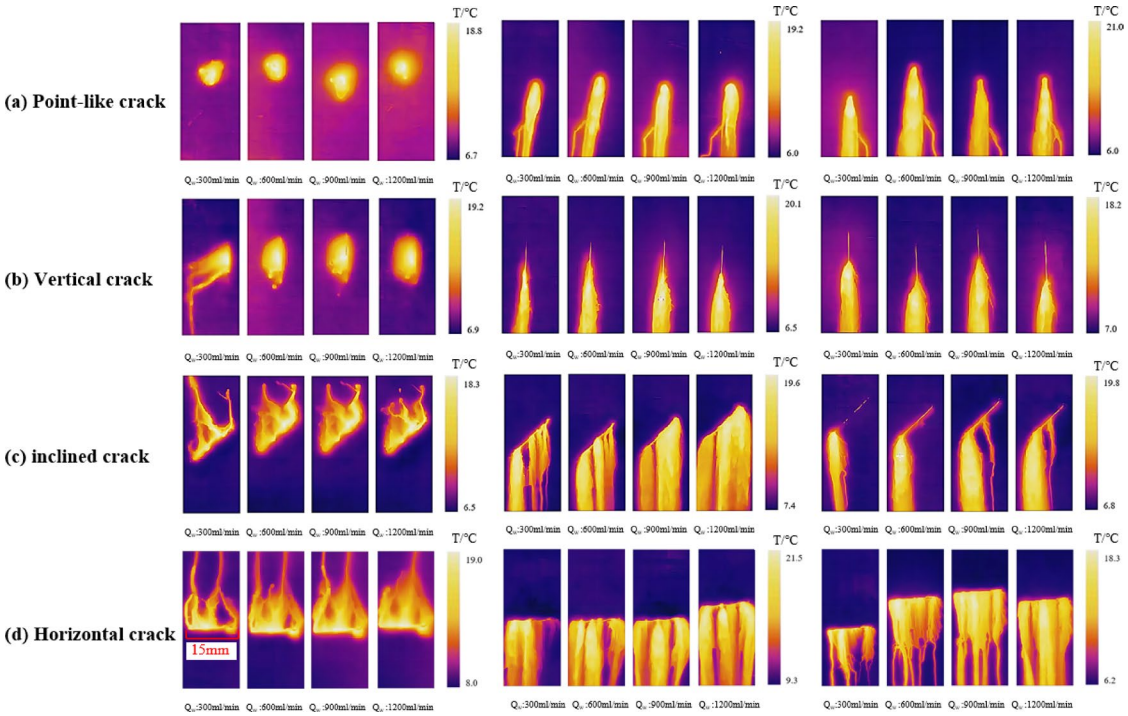

Fig. 6. Infrared images of seepage areas under various working conditions.

Geometric characteristics of seepage area with horizontal cracks

Infrared thermal images of the seepage area under horizontal crack conditions are shown in Fig. 6b. The seepage area of horizontal cracks at the vault is symmetrically distributed as a whole. Only one side has an obvious seepage area, with the outer contour of the main seepage area composed of an upper trapezoid and a lower rectangle. As the flow rate increases, the crack is filled with seepage water, but the outer contour of the seepage remains basically unchanged. When horizontal cracks are at the spandrel and haunch, the number of seepage points increases with the flow rate, and the seepage area also increases accordingly, presenting a waterfall shape. Under flow rate conditions above 300 mL/min, the image contour of seepage presents a rectangular distribution due to gravity.

Geometric characteristics of seepage area with vertical cracks

Infrared thermal images of the seepage area under vertical crack conditions are shown in Fig. 6c. The geometric image of the seepage area of vertical cracks at the vault finally presents a rice-grain shape; the geometric images of the seepage area at the spandrel and vault show a combined shape of linear, conical, and rectangular from top to bottom. The seepage area at the vault decreases with the increase of flow rate; the seepage area at the spandrel expands horizontally with the increase of flow rate; and the seepage area at the haunch remains basically unchanged with the increase of flow rate.

Geometric characteristics of seepage area with inclined cracks

Infrared thermal images of the seepage area under inclined crack conditions are shown in Fig. 6d. When the flow rate is less than 600 mL/min, the seepage area exudes linearly along the vertical direction of the crack on the vault surface. When the flow rate increases to 900 mL/min and 1200 mL/min, the seepage area shows a parallelogram distribution as a whole. In summary, the water outlet points of inclined cracks at different positions gradually increase with the increase of flow rate. The geometric image of seepage at the vault presents a parallelogram shape as a whole; the geometric image of seepage at the spandrel finally presents a right trapezoid shape; and the geometric image of seepage at the haunch presents a "kettle" shape as a whole.

Thus, the geometric characteristics of seepage areas formed by various cracks are summarized in Table 2.

Analysis of seepage area under different flow velocities

Image processing method

Based on Python language in PyCharm, the original infrared thermal images were processed as follows:

1 Grayscale processing of the original images, grayscale conversion adopts default weights (R:0.299, G:0.587, B:0.114), which complies with the CIE 1931 standard. This approach can effectively retain the temperature information of thermal images and avoid interference between color channels;

2 smoothing processing of the images using a discrete cosine transform-based image denoising method, the image is segmented into 8×8 pixel blocks, and each block undergoes DCT transformation (using cv2.dct()). A threshold ($T = 30$) is set to filter out high-frequency coefficients (coefficients below the threshold are set to zero), followed by image reconstruction via inverse DCT;

3 binarization processing of the images by threshold segmentation, the Otsu's method is used to automatically calculate the optimal threshold, maximizing the inter-class variance. This method is suitable for thermal images with a bimodal distribution of seepage areas and background areas;

4 statistical calculation of the ratio of white pixels to total pixels via the Opencv and numpy libraries to obtain accurate data of α. Finally, the seepage area A was obtained, and the ratio of the seepage area to the total specimen area was calculated using the following formula:

$$\alpha = \frac{A}{A_0} \tag{1}$$

where A0 is the actual area of the concrete specimen, and α is the ratio of the seepage area to the concrete plane area.

Analysis of seepage area with point-like cracks

The binarized images of seepage with point-like cracks were processed as above, and the ratio of the seepage area to the total area is shown in Table 3. The variation of the seepage ratio with flow rate for point-like cracks is shown in Fig. 7.

Comprehensive analysis of the table and figures shows that except for local errors, the seepage area ratio increases with the flow rate. Point-like cracks at the vault are more susceptible to seepage flow rate. When the flow rate Vw increases from 300 mL/min to 1200 mL/min, the seepage area ratio α increases from 9.8 to 14%.

Analysis of seepage area with horizontal cracks

The ratio of the seepage area to the total area for horizontal cracks is shown in Table 4.

The variation of the seepage ratio with flow rate for horizontal cracks is shown in Fig. 8. Comprehensive analysis of the table and figures shows that horizontal cracks at the haunch are more susceptible to seepage flow rate. When the flow rate Vw increases from 300 mL/min to 1200 mL/min, the seepage area ratio α increases from 20.56 to 49.14%.

Lining position	Crack type	Geometric characteristics summary
Vault	Point-like crack	Circular. The seepage area increases with the flow rate
	Inclined linear crack	Parallelogram
	Vertical linear crack	Rice-grain shape
	Horizontal linear crack	Upper trapezoid and lower rectangle
Spandrel	Point-like crack	Uniform-width strip distribution below the seepage point and semicircular at the top
	Inclined linear crack	Right trapezoid
	Vertical linear crack	Combined shape of linear, conical, and rectangular from top to bottom
	Horizontal linear crack	Waterfall shape
Haunch	Point-like crack	Semicircular distribution, presenting a mountain-like shape as a whole, and the width of the seepage area increases with the flow rate
	Inclined linear crack	"Kettle" shape
	Vertical linear crack	Combined shape of linear, conical, and rectangular from top to bottom
	Horizontal linear crack	Waterfall shape

Table 2. Summary of geometric characteristics of seepage areas for various cracks.

Condition	Lining position	Flow rate (mL/min)	Seepage area ratio (%)
1	Vault	300	9.80
2		600	11.89
3		900	11.49
4		1200	14.00
5	Spandrel	300	12.78
6		600	14.42
7		900	15.96
8		1200	16.19
9	Haunch	300	13.69
10		600	12.89
11		900	14.41
12		1200	13.69

Table 3. Statistical table of seepage area ratio for point-like cracks.

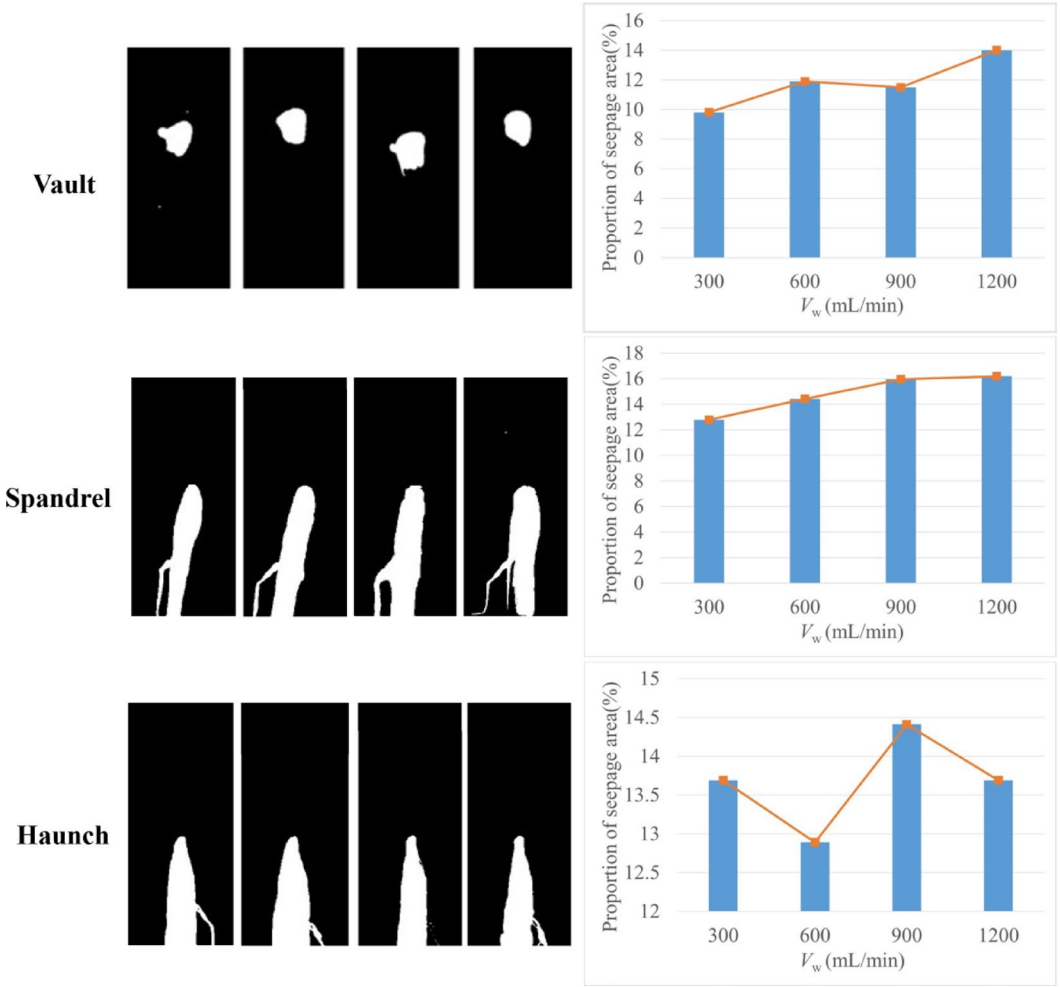

Fig. 7. Variation of seepage ratio with flow rate for point-like cracks.

Analysis of seepage area with vertical cracks

The ratio of the seepage area to the total area for vertical cracks is shown in Table 5.

The variation of the seepage ratio with flow rate for vertical cracks is shown in Fig. 9. Comprehensive analysis of the table and figures shows that vertical cracks at the spandrel are more susceptible to seepage flow rate. When the flow rate Vw increases from 300 mL/min to 1200 mL/min, the seepage area ratio α increases from 12.21 to 16.42%.

Condition	Lining position	Flow rate (mL/min)	Seepage area ratio (%)
1	Vault	300	24.85
2		600	30.87
3		900	33.78
4		1200	36.43
5	Spandrel	300	29.07
6		600	38.52
7		900	41.54
8		1200	51.16
9	Haunch	300	20.56
10		600	30.13
11		900	43.9
12		1200	49.14

Table 4. Statistical table of seepage area ratio for horizontal cracks.

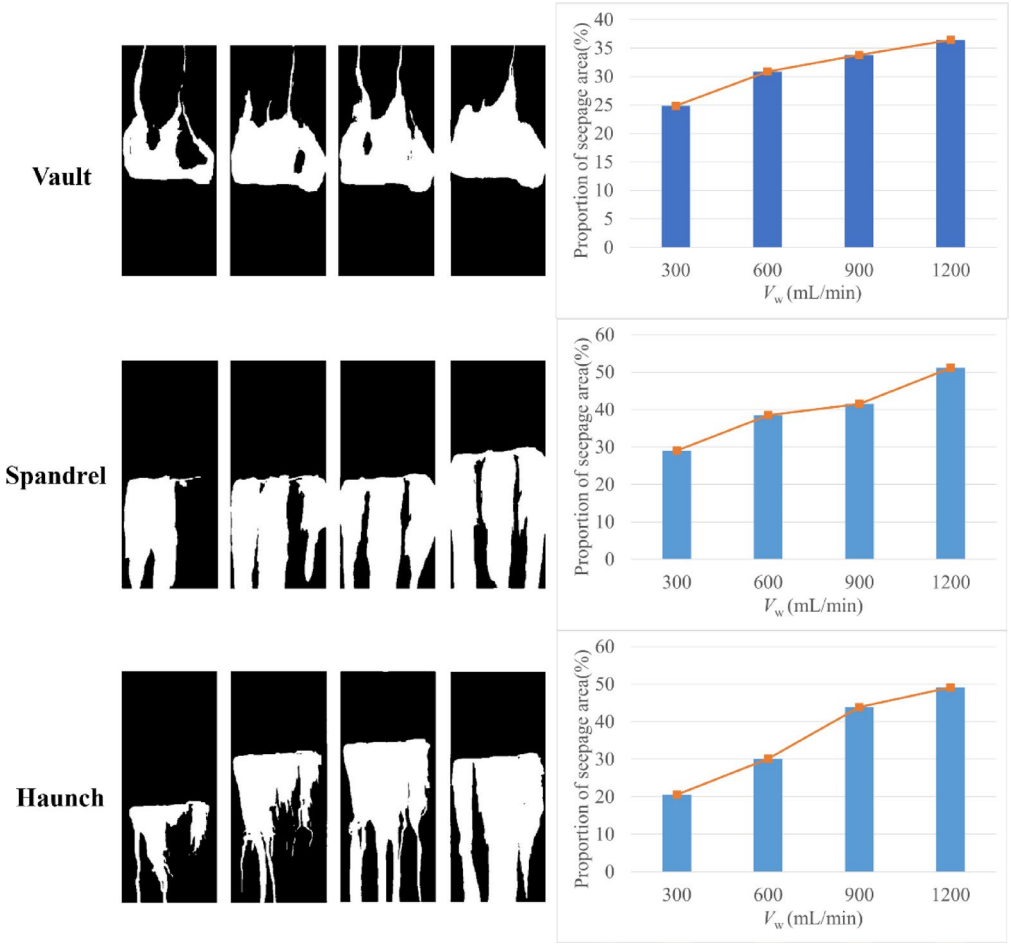

Fig. 8. Variation of seepage ratio with flow rate for horizontal cracks.

Analysis of seepage area with inclined cracks

The ratio of the seepage area to the total area for inclined cracks is shown in Table 6.

The variation of the seepage ratio with flow rate for inclined cracks is shown in Fig. 10. Comprehensive analysis of the table and figures shows that inclined cracks at the spandrel are more susceptible to seepage flow rate. When the flow rate Vw increases from 300 mL/min to 1200 mL/min, the seepage area ratio α increases from 27.11 to 59.30%.

In summary, the seepage area of all crack types increases with the flow rate. Point-like cracks and horizontal cracks are susceptible to seepage flow rate at the vault and haunch, respectively, while vertical and inclined cracks

Condition	Lining position	Flow rate (mL/min)	Seepage area ratio (%)
1	Vault	300	22.11
2		600	19.04
3		900	20.38
4		1200	23.08
5	Spandrel	300	12.21
6		600	15.26
7		900	14.98
8		1200	16.42
9	Haunch	300	11.38
10		600	14.65
11		900	13.60
12		1200	9.21

Table 5. Statistical table of seepage area ratio for vertical cracks.

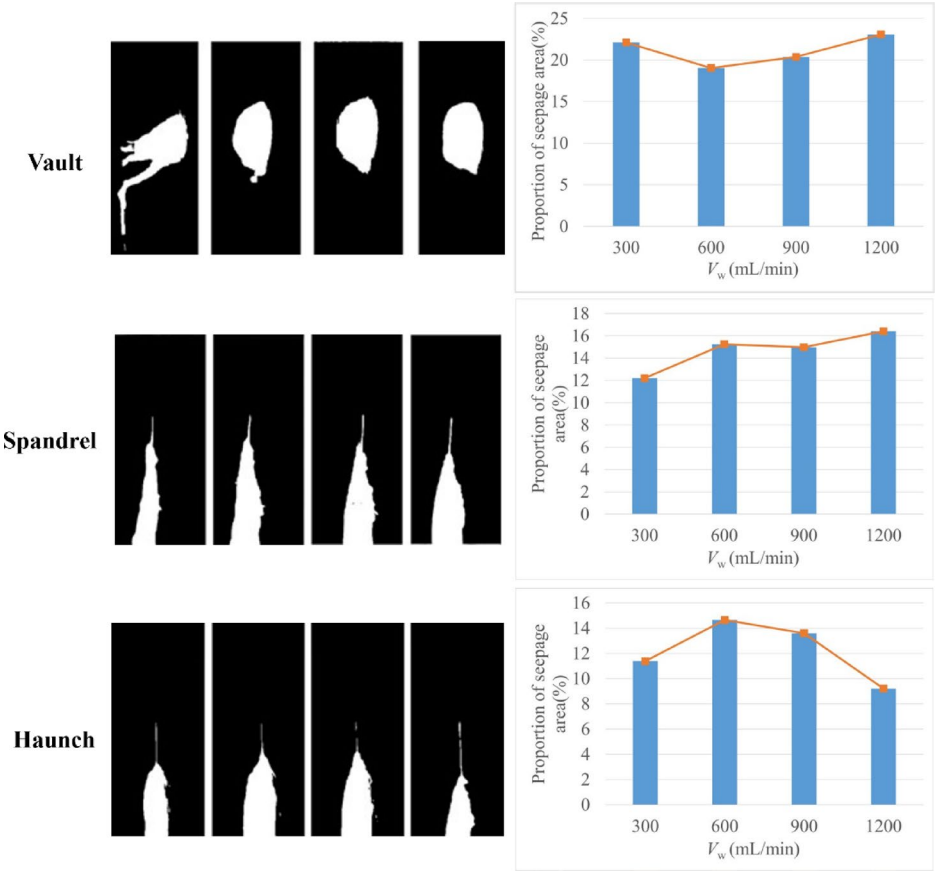

Fig. 9. Variation of seepage ratio with flow rate for vertical cracks.

are susceptible at the spandrel. The quantitative relationship between seepage area and flow rate can serve as the quantitative basis for "classification of seepage grades" specified in Technical Specification for Highway Tunnel Maintenance (JTG H12-2015)[20], addressing the limitation in existing specifications where only qualitative descriptions of seepage severity are provided.

Temperature field analysis of crack seepage

To rapidly and accurately determine the crack type of tunnel lining seepage, isothermal maps are generated from the temperature matrix of infrared thermal images to explore the temperature field distribution characteristics and centroid displacement trajectory of the seepage core area around lining cracks, ultimately achieving quantitative diagnostic analysis of structural defect areas.

Condition	Lining position	Flow rate (mL/min)	Seepage area ratio (%)
1	Vault	300	17.39
2		600	20.47
3		900	21.00
4		1200	19.25
5	Spandrel	300	27.11
6		600	30.18
7		900	41.18
8		1200	59.30
9	Haunch	300	21.20
10		600	23.28
11		900	28.43
12		1200	31.38

Table 6. Statistical table of seepage area ratio for inclined cracks.

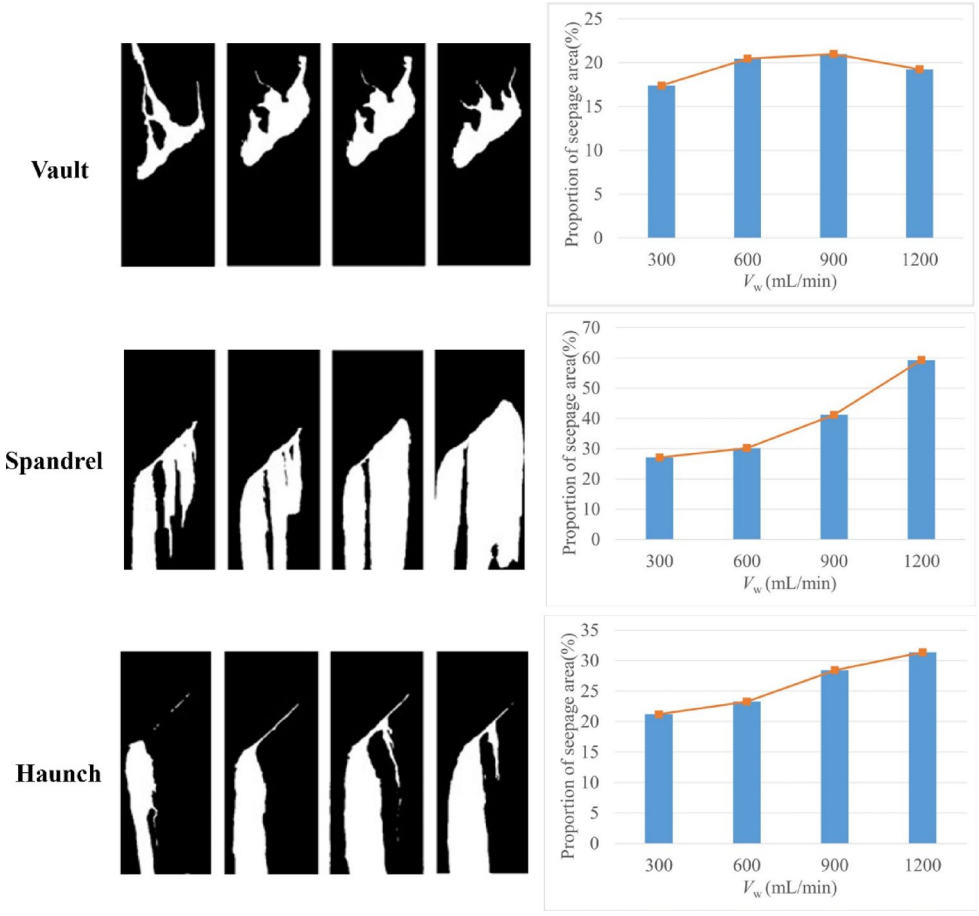

Fig. 10. Variation of seepage ratio with flow rate for inclined cracks.

Principle of centroid distance curve function

The centroid distance curve reflects the symmetry and structural changes of irregular shapes, making it particularly suitable for analyzing the influence of different crack types on seepage distribution. This section quantitatively analyzes the seepage morphology of different crack types by calculating the centroid distance curve of isotherms in the seepage core area. The calculation steps of the centroid distance curve are as follows:

(1) Isotherms in the seepage region show a decreasing temperature gradient from the inside out (diffusing from the seepage core to the surroundings). The first isotherm (innermost layer) only reflects the extreme temperature zone near the leakage point, with a too small range and vulnerability to local water flow disturbances; outer isotherms (e.g., the fifth and beyond) may include non-seepage background low-temperature zones (such

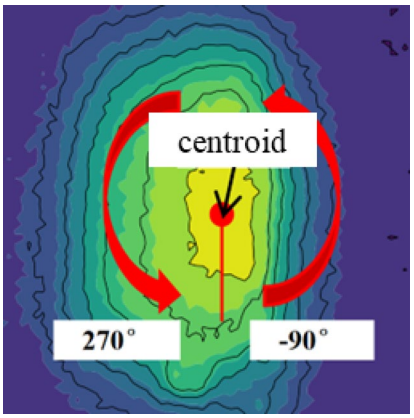

Fig. 11. Calculation sequence of isotherm sampling points.

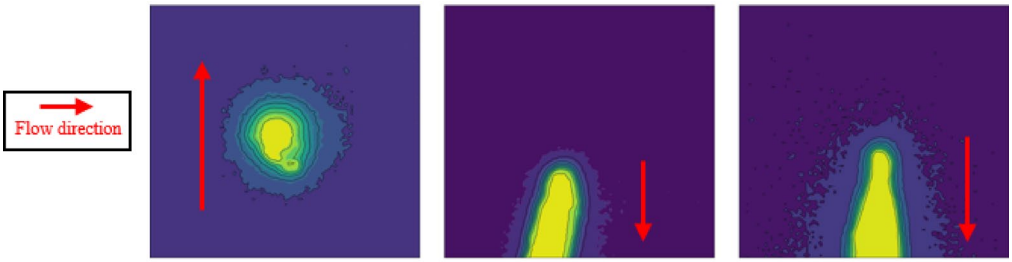

Fig. 12. Isothermal maps of seepage core area with point-like cracks.

as environmental condensation), leading to blurred boundaries. The third isotherm, located in the middle of the gradient, can both completely enclose the seepage core area (a stable temperature field dominated by flow rate and crack morphology) and exclude edge noise, thus better approximating the actual seepage influence range. Therefore, the third isotherm from high to low is selected as the contour of the seepage core area based on the isothermal map. The isothermal map defaults to the lower-left corner of the image as the origin of the coordinate system, with the side length of one pixel corresponding to the unit length in the coordinate system.

(2) Coordinates of sampling points on the isotherm contour are extracted to calculate the centroid position and the distance from each point to the centroid. The calculation formulas are shown in Eqs. (2) and (3)[30]:

$$X_c = \frac{\sum_{i=1}^{n} X_i}{n}, Y_c = \frac{\sum_{i=1}^{n} Y_i}{n} \tag{2}$$

$$D_i = \sqrt{[X_i - X_c]^2 + [Y_i - Y_c]^2} \tag{3}$$

where X_c is the abscissa of the centroid; Y_c is the ordinate of the centroid; n is the number of points on the isotherm; X_i and Y_i are the abscissa and ordinate of the sampling point, respectively; and D_i is the distance from the sampling point to the centroid.

(3) The centroid distance curve is plotted using the Matplotlib library in Python, with the angle as the abscissa (– 90° to 270°) and the distance as the ordinate. The calculation sequence of sampling points is shown in Fig. 11.

Temperature fields under different crack types

Isothermal maps are generated from the temperature matrix of exported infrared thermal images, and defect areas are analyzed. Corresponding isothermal maps are processed by Python programming, and a 100 × 100 pixel area near the defect position is cropped for analysis. The temperature difference between each isotherm is one-tenth of the temperature difference between the maximum and minimum temperatures in the image.

(1) Isothermal maps of seepage core area with point-like cracks

Isothermal maps of the seepage core area with point-like ceacks at different positions are shown in Fig. 12.

As shown in the figure, the isotherms of the seepage area with point-like cracks at the vault all present a regular circular shape, and the distance between isotherms increases from the seepage point to the periphery.

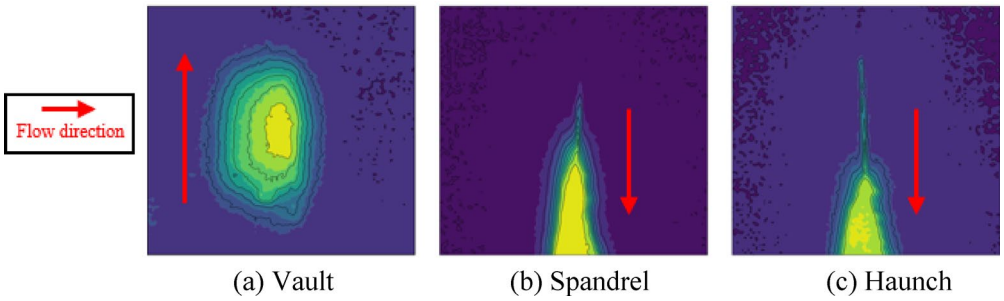

Fig. 13. Isothermal maps of seepage core area with vertical cracks.

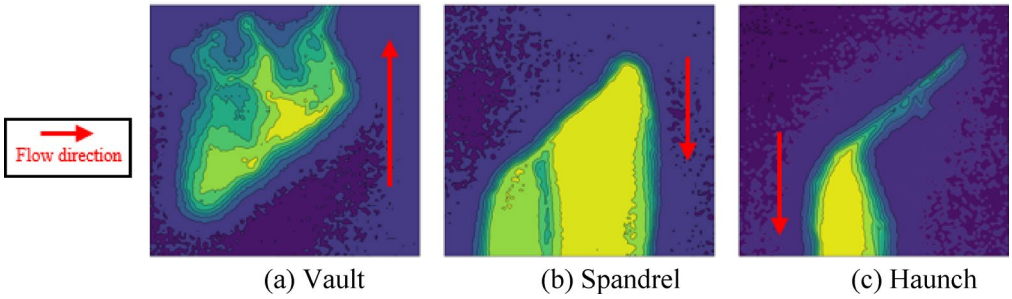

Fig. 14. Isothermal maps of seepage core area with inclined cracks.

The isotherms of the core seepage area with point-like defects at the spandrel and haunch are denser than those at the vault. The isotherms at the point-like defects are similar to the vault, forming a regular arc shape. In the area directly below the defects under the two working conditions, the isotherm contour at the spandrel is strip-shaped, with a width approximately equal to the arc diameter of the isotherm at the defect position, while the isotherm contour at the haunch is approximately an isosceles trapezoid, with an included angle of about 27° between the two waists. The seepage characteristics of point-like cracks arise from radial seepage of water flow from a single point to the surrounding area, forming a symmetrical heat exchange zone. The small crack opening limits the seepage range, resulting in a more concentrated temperature gradient. The vault is less affected by gravity, so the seepage area approximately exhibits circular diffusion; in contrast, the spandrel and haunch are more influenced by gravity, leading to downward extension from the point-like source.

(2) Isothermal maps of seepage core area with vertical cracks

Isothermal maps of the seepage core area with vertical cracks at different positions are shown in Fig. 13.

The isotherm contour of the seepage area with vertical cracks at the vault presents a rice-grain shape, with the distance between isotherms sparser on the left and denser on the right, indicating a large temperature gradient difference between the left and right sides. The isotherm contours of the core seepage area with vertical cracks at the spandrel and haunch are basically consistent with their geometric characteristics, showing a symmetrical pattern. The isotherms have an abrupt change in angle in the main water outlet area along the crack direction from top to bottom, with a mutation angle of about 30° at the spandrel and about 50° at the haunch. In the case of vertical cracks, the temperature field shows an elongated distribution along the crack direction. Due to gravity-driven water flow preferentially seeping in the vertical direction, the heat conduction path is extended, resulting in an additional slender temperature field line in the spandrel and haunch regions compared to point-like cracks.

(3) Isothermal maps of seepage core area with inclined cracks

Isothermal maps of the seepage core area with inclined cracks at different positions are shown in Fig. 14.

The isotherm contour of the seepage area with inclined cracks at the vault is an irregular pattern, but the lower right side of the isotherm contour presents a relatively regular straight line, with dense isotherms, corresponding to the crack position. The isotherm contour of the core seepage area with inclined cracks at the spandrel is a right trapezoid, with the densest isotherm spacing at the oblique waist, which is also the crack position. For the isothermal image of the core seepage area with inclined cracks at the haunch, the top of the isotherm contour has an obliquely protruding sharp corner, and the direction pointed by the corner is the crack dip. The asymmetrical temperature distribution in the case of inclined cracks is related to the crack inclination angle. When water seeps along the inclined direction, the gravitational component and crack orientation jointly affect the seepage velocity. The upstream side forms a more obvious low-temperature zone due to the longer water flow retention time.

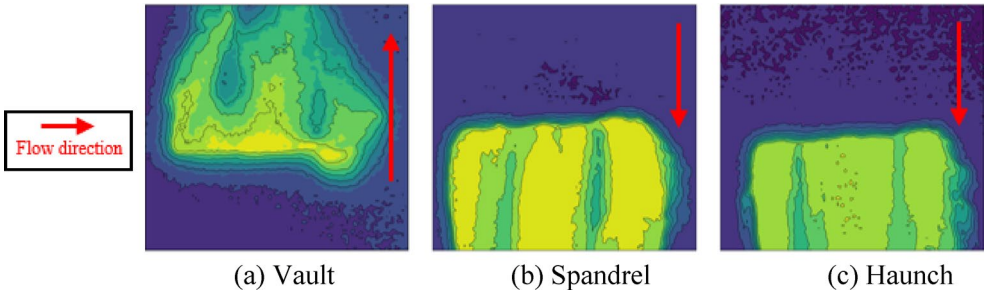

Fig. 15. Isothermal maps of seepage core area with horizontal cracks.

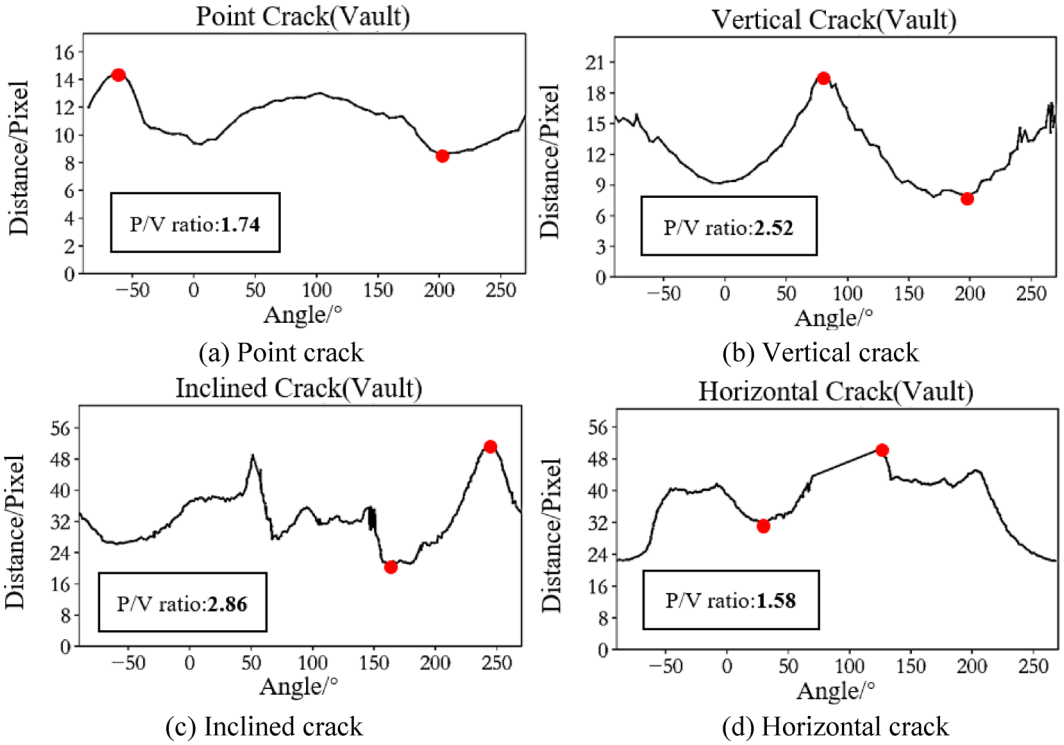

Fig. 16. Centroid distance curves of seepage with different morphologies at the vault.

(4) Isothermal maps of seepage core area with horizontal cracks

Isothermal maps of the seepage core area with horizontal cracks at different positions are shown in Fig. 15.

The innermost isotherm contour of the seepage area with horizontal cracks at the vault is generally a horizontal strip, and the enclosed area is approximately the range of the horizontal crack. The isotherm contours of the core seepage area with horizontal cracks at the spandrel and haunch are symmetrically distributed as a whole, presenting an approximate rectangular shape. In the case of horizontal cracks, as the water flow is less affected by gravity, it diffuses uniformly along the lateral direction of the crack, leading to more sufficient heat exchange and thus a more uniform temperature distribution.

In summary, the isotherm morphologies of the seepage core area under different crack types show significant differences. Compared with infrared images, isothermal maps can reveal the temperature distribution and variation of the seepage area. By analyzing the geometric shape parameters of isotherms in the isothermal map, the corresponding crack morphology and position can be preliminarily determined.

Analysis of centroid distance function curves

Using the calculation method in Sect. 3.2.1, the centroid distance function curves of isotherms at different positions are obtained from the above isothermal maps.

Analysis of centroid distance curves at the vault

Centroid distance curves of different crack types at the vault are shown in Fig. 16. Figure 16a is the centroid distance curve of point-like defects, which is relatively gentle without obvious peaks. Figure 16b is the centroid

distance curve of vertical cracks, with a single peak near 75°. The slope transition at the peak is smooth, without significant mutation, and the curvatures on both sides of the peak are positive, showing an upward convex shape. Figure 16c is the centroid distance curve of inclined cracks, with two obvious peaks. The curve between the two peaks shows irregular fluctuations, with peaks near 50° and 250°. The slope at the 50° peak has a mutation, while the slope at the 275° peak transitions smoothly. Figure 16d is the centroid distance curve of horizontal cracks, with two valleys near 35° and 275°. The slope at the 35° valley has a mutation, and the slope at the 275° valley transitions smoothly.

Analysis of centroid distance curves at the spandrel

Centroid distance curves of different crack types at the spandrel are shown in Fig. 17. Figure 17a–c are the centroid distance curves of point-like defects, vertical cracks, and inclined cracks, respectively. The curves of the three defects all show a single-peak shape. The peaks of point-like defects and vertical cracks are both near 80°; the curvatures on both sides of the peak of point-like defects are negative; the curvatures on both sides of the peak of vertical cracks are positive, and the slope at the peak has a mutation. The peak of inclined cracks is near 60°, the curvatures on both sides of the peak are negative, and the slope transition at the peak is smooth. Figure 17(d) is the centroid distance curve of horizontal cracks, showing a single-valley shape overall, with the valley position near 100°.

Analysis of centroid distance curves at the haunch

Centroid distance curves of different crack types at the haunch are shown in Fig. 18. The overall morphology of the centroid distance curves for different defects at the haunch is the same as that at the spandrel, but there are local differences. For point-like defects, the slope of the curve on both sides of the peak at the haunch is generally greater than that at the spandrel. For vertical cracks, the overall slope of the curve on both sides of the peak at the haunch is smaller than that at the spandrel. For inclined cracks, the left side of the peak at the haunch approaches a straight line with a 90° angle to the horizontal, with a larger slope than at the spandrel, and there is a slope mutation on both sides of the peak compared with the haunch. The curves of horizontal cracks at the spandrel and haunch have no significant difference, but the angular range of the valley at the haunch is slightly larger than that at the spandrel.

In summary, the centroid distance curves of seepage corresponding to different defects at different positions show significant differences. The overall morphology of the centroid distance curve of seepage (such as peak position, number of peaks, etc.) and curve shape parameters (such as curve slope, curve curvature, etc.) and their variation can be used to further determine the corresponding lining crack morphology and its position.

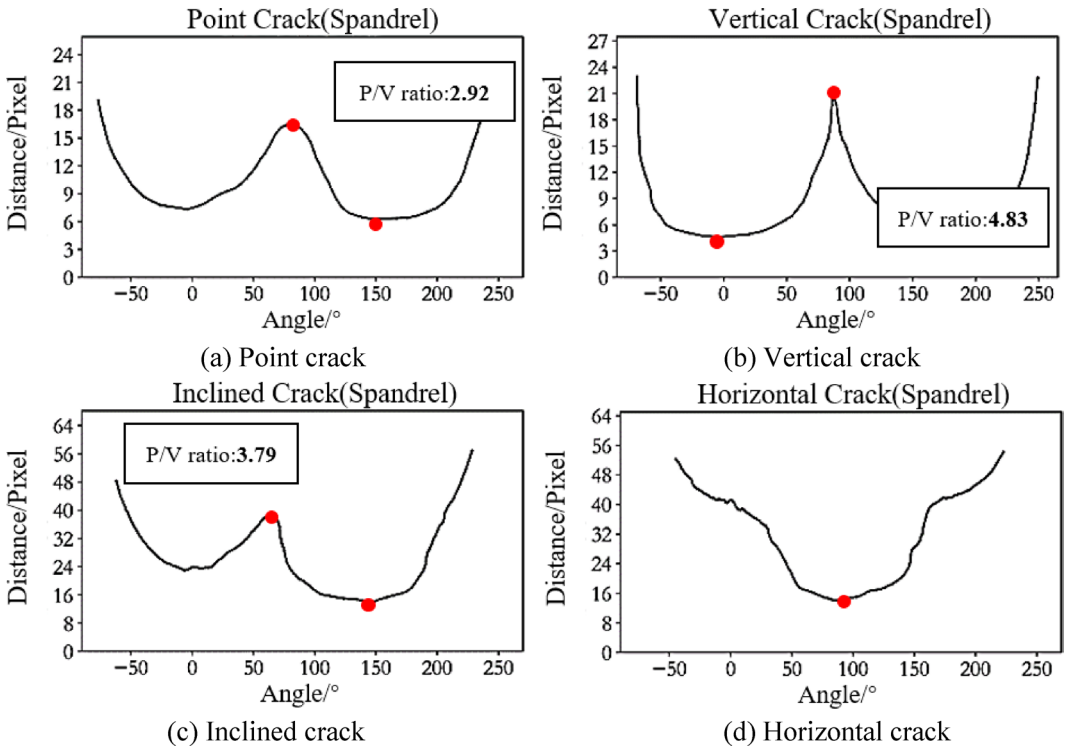

Fig. 17. Centroid distance curves of seepage with different morphologies at the spandrel.

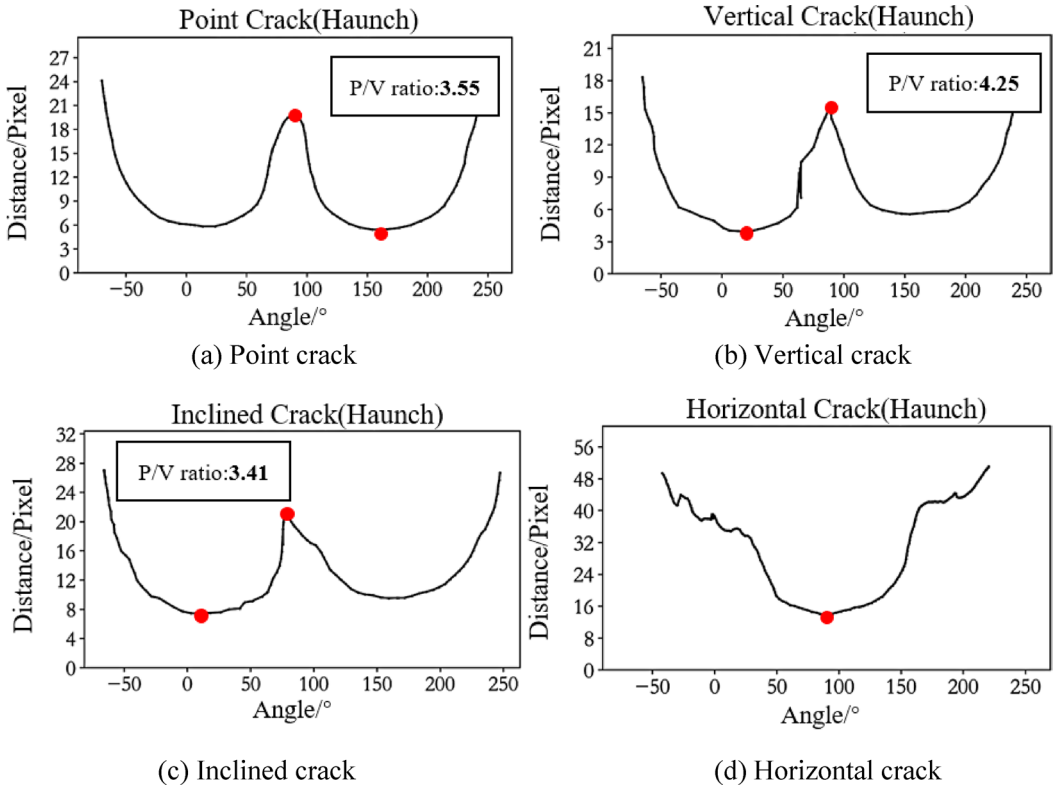

Fig. 18. Centroid distance curves of seepage with different morphologies at the haunch.

Conclusions

This study simulated seepage scenarios at different positions of tunnel linings and deeply explored the characteristics of infrared thermal images of seepage areas under different crack types and flow velocities. The main conclusions are as follows:

(1) The form and location of cracks determine the geometric characteristics of water seepage areas. The geometric characteristics of various types of cracks and different seepage regions have been systematically summarized. Additionally, the quantitative relationship between seepage area and flow rate has been discussed, which can serve as a quantitative basis for "seepage grade classification" and address the limitation in existing regulations where "only qualitative descriptions of seepage severity are provided".

(2) The centroid distance curves of different crack types in the vault area show significant differences. The curve of point-like cracks is gentle without obvious characteristics; the vertical crack shows a single peak near 75°, with positive curvature and smooth transition; the inclined crack forms double peaks at approximately 50° and 250°, with the former having a slope mutation and the latter smooth transition; the horizontal crack shows double valleys near 35° and 275°, with varying slope changes. These characteristics enable precise identification of vault crack types.

(3) In the spandrel area, the point-like crack forms a single peak near 80° with negative curvature; the vertical crack also forms a peak at 80°, but with positive curvature and slope mutation; the inclined crack has a peak near 60°, with negative curvature and stable slope change; the horizontal crack forms a single valley near 100°. The position, curvature, and slope characteristics of peaks/valleys effectively identify spandrel crack morphologies.

(4) The overall morphology of the haunch curve is similar to that of the spandrel, but differences exist in slope and transition characteristics. The slopes on both sides of the point-like crack peak are larger; the vertical crack has smaller slopes; the left side of the inclined crack peak is nearly vertical, with obvious slope mutation, indicating that the crack direction affects local deformation; the horizontal crack valley has a wider range, reflecting seepage expansion differences. These differences reflect the coupling effect between crack morphology and structural position, contributing to improved accuracy in crack localization and diagnosis.

(5) This research's single-point or linear crack models exhibit discrepancies with actual complex crack networks; moreover, they have not addressed seepage and temperature characteristics in the 3D thickness direction of the lining. Future research will leverage existing main crack features and centroid curve parameters, extending to the identification of complex cracks through feature fusion and machine learning. It will also investigate characteristics in the 3D thickness direction by coupling surface infrared data with 3D heat transfer models, integrating multispectral technology, and conducting field measurement calibration, thereby offering more comprehensive support for practical defect diagnosis.

Data availability

Data available on request from the corresponding author, Yimin Wu.

Received: 15 June 2025; Accepted: 30 July 2025
Published online: 20 August 2025

References

1. Yang, Q. *et al. Development and verification of a vertical graphene sensor for tunnel leakage monitoring* (ACS applied materials & amp; interfaces, 2024).
2. Teng, T. *et al.* In situ nuclear magnetic resonance observation of pore fractures and permeability evolution in rock and coal under triaxial compression. *J. Energy Eng.* 151(4) (2025).
3. Gu, Y. *et al.* Cost-effective image recognition of water leakage in metro tunnels using self-supervised learning. *Autom. Construct.* 167105678–105678 (2024).
4. Liu, Y. *et al.* Study on leakage assessment and stability analysis of water level changes in tunnels near reservoirs. *Water* **16**(17):2378–2378 (2024).
5. Zhengzheng, C. *et al.* Diffusion evolution rules of grouting slurry in mining-induced cracks in overlying strata. *Rock Mechan. Rock* **58**(6):1–20 (2025).
6. Liu, K. Y. *et al.* Development of a water leakage model test system and investigation of the water leakage behavior in subsea shield tunnels during operation. *Measurement* 233114691 (2024).
7. Xu, P. *et al.* Effect of polymeric aluminum chloride waste residue and citric acid on the properties of magnesium oxychloride cement. *J. Building Eng.* 101111864–101111864. (2025).
8. Park, D. *Numerical investigation on the effect of water leakage on the ground surface settlement and tunnel stability*146105656 (Tunnelling and Underground Space Technology incorporating Trenchless Technology Research, 2024).
9. Xi, C. *et al.* Intelligent identification of tunnel water leakage based on super-resolution reconstruction and triple attention. *Measurement* 225114009. (2024).
10. Chen, W. *et al. Towards automated 3D evaluation of water leakage on a tunnel face via improved gan and self-attention DL model*142 (Tunnelling and Underground Space Technology incorporating Trenchless Technology Research, 2023).
11. Xu, Q. *et al.* Numerical simulation and analysis of the causes and distribution of secondary lining cracks in overlapping railway tunnels.*Appl. Sci.* **13**(11) (2023).
12. Lei, T. *et al.* A lightweight metro tunnel water leakage identification algorithm via machine vision. *Eng. Failure Anal.* **150**, 107327 (2023).
13. Zhao, L. *et al.* An adaptive multitask network for detecting the region of water leakage in tunnels. *Appl. Sci.* **13**(10) (2023).
14. Technical specification for construction of highway asphalt pavements (JTG F40-2004).
15. Peng, G. *et al.* ACPA-Net: atrous channel pyramid attention network for segmentation of leakage in rail tunnel linings. *Electronics* **12**(2):255–255 (2023).
16. Jian, L. *et al. Research on infrared feature recognition algorithm for water leakage in highway tunnels* (Shandong University (China), 2022).
17. Hawley, C. J. & Gräbe, P. J. Water leakage mapping in concrete railway tunnels using lidar generated point clouds. *Constr. Build. Mater.* **361**, 129644 (2022).
18. Dongwei, Q. *et al.* Hybrid-supervised-learning-based automatic image segmentation for water leakage in subway tunnels. *Appl. Sci.* **12**(22):11799–11799 (2022).
19. Xin, Z., ,Guoqiang, L. & ,Qun, N. Rapid detection method of local leakage water in shield tunnel based on three-dimensional laser. *Int. J. New. Dev. Eng. Soc.* **6.0**(3.0) (2022).
20. Technical specification for highway tunnel maintenance (JTG H12-(2015)).
21. Ke, M. *et al.* Water leakage and crack identification in tunnels based on transfer-learning and convolutional neural networks. *Water* **14**(9):1462–1462 (2022).
22. Haozheng, W. *et al.* Design of fast acquisition system and analysis of geometric feature for highway tunnel lining cracks based on machine vision. *Appl. Sci.* **12** (5), 2516–2516 (2022).
23. Chengjun, H., Xinrui, L. & Ming, W. Analysis of crack formation and growth in tunnel linings using double-k fracture criterion. *Appl. Sci.* **12** (3), 1064–1064 (2022).
24. Yadong, X. *et al.* An optimization strategy to improve the deep learning-based recognition model of leakage in shield tunnels. *Comput.-Aided Civil Infrastruct. Eng.* **37** (3), 386–402 (2021).
25. Xiaolong, C. *et al.* Automatic detection of shield tunnel leakages based on terrestrial mobile lidar intensity images using deep learning. *IEEE Access* 955300–55310 (2021).
26. Shijie, Z. *et al.* The crucial techniques of water leakage treatment in operating highway tunnel. *IOP Conf. Ser.: Earth Environ. Sci.* **525**(1):012160 (2020).
27. Jianxun, S. *et al.* Study on multi-arch tunnel leakage disease with influence of rainfall and groundwater change. *IOP Conf. Ser.: Mater. Sci. Eng.* 741012101–012101. (2020).
28. Hangbin, W. *et al.* Extraction of water seepage in subway tunnels based on infrared thermal imaging. *Eng. Surv.* **47** (02), 44–49 (2019).
29. Haitao, D., Hongwei, H. & Yadong, X. Experimental study on the influencing factors of infrared radiation characteristics of tunnel lining water seepage. *J. Rock. Mech. Eng.*, **30**(12):2426–2434 (2011) .
30. Aichen, Z. *et al.* Experimental study on infrared feature recognition of water seepage in cracked tunnel lining. *J. Southeast. Univ. (Natural Sci. Edition)*, **52**(01):109–116 (2022) .
31. Muhammad, N. Z. *et al.* Waterproof performance of concrete: a critical review on implemented approaches. *Constr. Build. Mater.* **101**, 80–90. https://doi.org/10.1016/j.conbuildmat.2015.10.048 (2015).
32. Zhou, Z. Q. *et al.* An optimal classification method for risk assessment of water inrush in karst tunnels based on grey system theory. *Geomech. Eng.* **8** (5), 631–647. https://doi.org/10.12989/gae.2015.8.5.631 (2015).
33. Sanudo, R. *et al.* Drainage in railways. *Constr. Build. Mater.* **210**, 391–412 (2019).

Author contributions

Conceptualization, Yimin Wu, Zhijian Wu; methodology, Yimin Wu, Zhijian Wu; validation, Guangzheng Zhuang, Hua Wu; investigation, Hua Wu; resources, Zhijian Wu; data curation, Yichen Peng; writing-original draft preparation, Haiping Wu; writing—review and editing, Yichen Peng; visualization, Renjie Song; project administration, Zhijian Wu. All authors have read and agreed to the published version of the manuscript.

Funding

This research is funded by Jiangxi Communications Investment Group Co., Ltd. through the scientific research

project of China Highway Association and Anhui Transport Consulting & Design Institute Co., Ltd.

Declarations

Competing interests
The authors declare no competing interests.

Additional information
Correspondence and requests for materials should be addressed to Y.W.

Reprints and permissions information is available at www.nature.com/reprints.

Publisher's note Springer Nature remains neutral with regard to jurisdictional claims in published maps and institutional affiliations.